COMPUTERIZED TOMOGRAPHY

Tomography refers to the synthesis of sectional images or slices from external measurements of a spatially varying function. Line integrals are the most common external measures, which are also known as *projections*. Availability of multiple projections at different orientations allows accurate recovery of the originating function. Because practical implementation of tomography typically requires large amounts of data and calculations, modern computing technologies are important. Computerized tomography (CT) is interdisciplinary, involving electrical and electronics engineering, mathematics, computer science, physics, mechanics, and biomedical sciences.

CT applications are numerous and diverse. Due to its penetrating power and contrast mechanism, X-ray CT has found wide use in medical imaging, industrial nondestructive evaluation, airport screening, and microtomography. In nuclear medicine, a radiating source distribution inside a patient is observed as the intensity of singly (single photon emission computerized tomography, SPECT) or pairwise (positron emission tomography, PET) emitted photons detected outside the patient. If the attenuation of the body is neglected, measures are line integrals of the source distribution. In magnetic resonance imaging (MRI), radio-frequency electromagnetic waves are generated by changes of orientation and magnitude of internal magnetic fields, which are produced by spinning nuclei in external magnetic fields. The radio signals are detected by an antenna to provide information on the Fourier transform of a cross section, which is directly related to line integrals of the nuclei density. In transmission electron microscopy, an electron beam penetrates a specimen over a limited angular range to collect projections. In ionospheric tomography, the total electron content is measured between an orbiting satellite and several ground stations. In geophysics, phase shifts of electromagnetic signals are detected for spatial reconstruction of the electrical conductivity and dielectric permittivity of the subsurface. In oceanography, acoustic transmission from a single source suspended from a ship to sonobuoys dropped from the air are recorded for mapping of ocean sound speed. In astronomy, the sun can be observed using an antenna with a parabolic section, and an integral signal is recorded over a thin strip of the radio emission distribution. By moving the antenna, the integrals are obtained over different strips for reconstruction of the ratio emission distribution. CT principles are also applied in optical tomography, diffraction tomography, and other areas.

The CT literature is large and growing. Historically, three contributors are most important: Radon, Hounsfield, and Cormack. Reconstruction of a function from its projections was first formulated by Radon in 1917 (1). The first experimental X-ray CT scanner was fabricated and tested by Hounsfield in 1972 (2). An important contribution to mathematics of X-ray CT was made by Cormack (3,4). Hounsfield and Cormack shared the 1979 Nobel Prize for medicine.

In this article, we introduce physical and mathematical principles of CT, describe practical reconstruction algorithms for various imaging geometries, and discuss image quality. We focus on X-ray CT, the most prominent example of CT, which has been greatly advanced over the past two decades, has benefited millions of patients, and still represents an important research area. CT in medical and industrial applications is now a worldwide major industry.

CT PRINCIPLES

The principles of CT are conceptually simple. Physically, X rays can traverse a cross section of an object along straight lines, can be attenuated by the object, and can be detected outside it. During CT scanning, the cross section is probed with X rays from various directions, and attenuated signals are recorded and converted to projections of the linear attenuation coefficient distribution of the cross section. These X-ray shadows are directly related to the Fourier transform of the cross section, and they can be processed to reconstruct the cross section.

Projection Measurement

Let us consider the simplest case, a single block of homogeneous tissue and a monochromatic beam of X rays. The linear attenuation coefficient μ is defined by

$$S_a = S_i \exp[-\mu \Delta l] \tag{1}$$

where Δl is the length of the block, and S_i and S_a are incident and attenuated intensities of the X ray, respectively. Let

$\mu(x, y)$ denote the sectional attenuation variation. For an infinitely thin beam of monochromatic X rays, the detected intensity of the X ray along a straight line L is expressed as

$$S_{\mathrm{a}} = S_{\mathrm{i}} \exp\left[-\int_L \mu(x,y)\,dl\right] \tag{2}$$

as shown in Fig. 1. The line integral of $\mu(x,y)$ along L can be found as follows:

$$d_{\mathrm{p}}(\theta,t) = \ln\left(\frac{S_{\mathrm{i}}}{S_{\mathrm{a}}}\right), \qquad 0 \le \theta < \pi, \quad -\infty < t < \infty \tag{3}$$

where p denotes parallel-beam geometry and θ and t represent the projection angle and the detector position, respectively. Actually, θ and t are polar coordinates of the perpendicular vector from the center of object to the X ray. For a fixed θ, $d_{\mathrm{p}}(\theta, t)$ is also referred to as a projection. Because incremental attenuations are summed along X rays in the projection process, and variations of $\mu(x,y)$ are superimposed along X rays, it is impossible to reconstruct $\mu(x,y)$ from a single projection. However, as we will see in the following section, $\mu(x,y)$ can be exactly reconstructed if all projections, $d_{\mathrm{p}}(\theta, t)$, are available. Note that if the X-ray intensity is low, statistical fluctuation must be taken into account.

Technologies of X-ray sources, detectors, and collimators are critical to data acquisition. Currently, a diagnostic type X-ray tube is used as the radiation source of the medical CT scanners. The tube is operated with high-frequency power, a rotating anode disk, and a small focal spot down to 0.6 mm. The disk is usually made of a rhenium, tungsten, and molybdenum (RTM) alloy and can be rotated at a speed of up to 10,000 rotations per minute. Radiation from these X-ray tubes is polychromatic, and it is narrowed by appropriate filtration to have a more concentrated spectrum. Pre- and post-patient collimators restrict the filtered X-ray beam to the anatomy of interest. CT detectors convert attenuated X-ray signals into electrical signals. There are two types of detectors: scintillation detectors and xenon detectors. In the scintillation detector, scintillation crystals will produce light if they are exposed to ionizing radiation. The light is then transformed into an electric signal by a photomultiplier or a silicon photodiode (also called solid-state photodiode). In the xenon detector, a xenon gas ionization chamber is used to measure incoming radiation, where interaction of X-ray photons and gas atoms produces electron–ion pairs. These electron–ion pairs form a current between the anode and the cathode when a high voltage is applied. The intensity of this current is proportional to the intensity of the incoming radiation. In terms of the conversion efficiency, the scintillation detector is better.

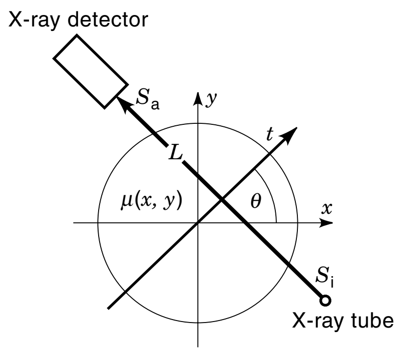

Figure 1. Line integrals of $\mu(x, y)$, the linear attenuation of an object, can be determined from S_{i} and S_{a}, incident and attenuated intensities of the X ray along a path L.

Fourier Slice Theorem

In tomography, various geometries are used to collect projection data, as detailed below. For simplicity, we introduce image reconstruction with the 2-D parallel-beam geometry. The 2-D Fourier transform of an image function $i(x,y)$ is defined as

$$I(u,v) = \int_{-\infty}^{\infty}\int_{-\infty}^{\infty} i(x,y)e^{-j2\pi(ux+vy)}\,dx\,dy \tag{4}$$

Restricting $I(u, v)$ to the line defined by $v = 0$, we have

$$I(u,0) = \int_{-\infty}^{\infty}\int_{-\infty}^{\infty} i(x,y)e^{-j2\pi ux}\,dx\,dy \tag{5}$$

Because the phase is no longer dependent on y, the integral can be split into two parts:

$$I(u,0) = \int_{-\infty}^{\infty}\left[\int_{-\infty}^{\infty} i(x,y)\,dy\right]e^{-j2\pi ux}\,dx \tag{6}$$

The term in brackets is recognized as the projection along lines of constant x,

$$d_{\mathrm{p}}(0,x) = \int_{-\infty}^{\infty} i(x,y)\,dy \tag{7}$$

that is,

$$I(u,0) = \int_{-\infty}^{\infty} d_{\mathrm{p}}(0,x)e^{-j2\pi ux}\,dx \tag{8}$$

In other words, the Fourier transform of the vertical projection of an image is the horizontal radial profile of the 2-D Fourier transform of the image.

This relationship can be generalized for any projection orientation. By the nature of the Fourier transform, if an image $i(x,y)$ is rotated by an angle with respect to the x axis, the Fourier transform $I(u,v)$ will be correspondingly rotated by the same angle with respect to the u axis. Therefore, the Fourier transform of a projection along the lines that make an angle $\theta + 90°$ with respect to the x axis depicts the Fourier transform of the image along the radial line that makes an angle θ. This relationship is illustrated in Fig. 2 and is referred to as the Fourier slice theorem; mathematically,

$$D_{\mathrm{p}}(\theta,w) = I(w\cos\theta, w\sin\theta) \tag{9}$$

where $D_{\mathrm{p}}(\theta, w)$ is the Fourier transform of $d_{\mathrm{p}}(\theta, t)$ with respect to t.

In n dimensions, we define the Radon transform R_n of a function $i(\vec{x})$ in the Schwartz space as the set of its integrals over the $(n-1)$-dimensional hyperplanes. Let $\vec{\theta}$ be a vector defined on the $(n-1)$-dimensional unit sphere, and let s be a real number:

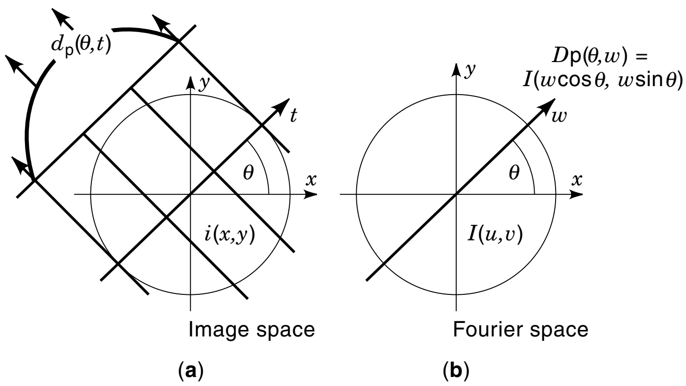

Figure 2. Fourier slice theorem. (a) Fourier transform of a projection at an angle θ corresponds to (b) a radial profile at the same angle in the Fourier space.

$$R_n(\vec{\theta}, s) = \int_{\vec{x}\cdot\vec{\theta}=s} i(\vec{x})\, d\vec{x} \tag{10}$$

R_n is an even function, that is, $R_n(-\vec{\theta},\ -s) = R_n(\vec{\theta},\ s)$. The generalized Fourier slice theorem (5) states that the Fourier transform of $R_n(\vec{\theta},\ s)$ with respect to s equals $I(\vec{\theta},\ w)$.

The Fourier slice theorem plays a fundamental role, because it relates Radon data to a radial profile in the Fourier space. In the "complete" case where all Radon data are available or derivable, the corresponding radial lines will cover the entire Fourier space. Then, the image can be reconstructed using the inverse Fourier transform. In practice, complete projection data are discretely sampled; and quantization error, nonlinearities, noise, and other nonidealities are present. There are many algorithms for image reconstruction from projections, and we will explain the most important ones below.

Imaging Geometries

The imaging geometry of CT is of fundamental importance in designing a CT scanner system and a reconstruction algorithm. Popular types of CT geometries are summarized in Fig. 3. The first generation scanner is characterized by an assembly of an X-ray source and a single detector [Fig. 3(a)]. For a given projection angle, a parallel-beam projection profile is collected while the assembly is translated along a straight line segment. The projection angle can be controlled by rotation of the assembly. The second generation scanner is also in a translation–rotation mode, but multiple detectors are employed that extend a small fan-beam angle [Fig. 3(b)]. The third-generation scanner utilizes many more detectors and has a much wider fan-beam angle so that X rays from an X-ray source cover the entire cross section to be reconstructed [Fig. 3(c)]. Therefore, there is no need for translation of the source-detector assembly. In other words, the assembly works in a rotation fashion. In the fourth-generation design, detectors are distributed along a full circle, and only an X-ray source is orbited [Fig. 3(d)].

Fan-beam spiral/helical scanning is the standard medical CT mode. Spiral CT is implemented by simultaneous patient translation, gantry rotation, and data acquisition [Fig. 3(e)] (6–8). The slip-ring is a key component for spiral scanning, in which a brush slides along a ring as the x-ray source rotates so that electrical energy is continuously supplied. The maximum scanning time with the slip-ring technique is determined by the thermal limitation of the X-ray tube. Twin-beam spiral CT is based on helical scanning of two contiguous transaxial sections (9).

Traditionally, volumetric image reconstruction is achieved by scanning a series of cross sections and by stacking these slices. In cone-beam geometry, instead of scanning an object with a planar beam of X rays, the entire object is illuminated with a point source, and the X-ray flux is measured on a detector plane behind the object [Fig. 3(f)]. The primary advantages of cone-beam geometry include reduced data acquisition time, improved image resolution, and optimized photon utilization.

Two unique CT scanners deserve special mentions: the dynamic spatial reconstructor (DSR) (10) and the electron-beam CT scanner (11). Both can complete data acquisition in a fraction of a second and can enable cardiac imaging. In the SDR, 28 X-ray tubes are arranged in a semicircle in a circular gantry. Projections are formed on the fluorescent screen arc, scanned via multiple imaging chains, and reconstructed volumetrically. In the electron-beam scanner, conventional mechanical rotation of an X-ray source is replaced by electromagnetic steering of an electron-beam around one of four semicircular tungsten targets of 210° and 90 cm in radius. Projections are measured by two stationary detector rings of 216° and 67.5 cm in radius.

Fig. 4 shows an Elscint twin-beam spiral CT scanner. Fig. 5 reveals an inside view of a Siemens spiral CT gantry. Fig. 6 is a transaxial slice of a human head reconstructed by a Picker spiral CT scanner. Fig. 7 contains a photo and a schematic drawing of the DSR.

IMAGE RECONSTRUCTION

There are two major classes of CT image reconstruction algorithms: filtered backprojection and iterative reconstruction. Filtered backprojection is the most popular, since it is accurate and amenable to fast implementation. Iterative reconstruction has significant potential for increased use in future, because it provides a solid framework for handling incomplete and noisy projection data.

Filtered Backprojection

The filtered backprojection algorithms are described for parallel-beam, fan-beam, and cone-beam cases in this section.

Parallel-Beam Reconstruction. With the inverse Fourier transform, an image $i(x, y)$ can be expressed as

$$i(x, y) = \int_{-\infty}^{\infty}\int_{-\infty}^{\infty} I(u, v)e^{j2\pi(ux+vy)}\, du\, dv \tag{11}$$

Let

$$u = w\cos\theta, \qquad v = w\sin\theta \tag{12}$$

we have

$$i(x, y) = \int_{0}^{2\pi}\int_{0}^{\infty} I(\theta, w)e^{j2\pi(x\cos\theta+y\sin\theta)w} w\, dw\, d\theta \tag{13}$$

Because

$$I(\theta + \pi, w) = I(\theta, -w) \tag{14}$$

we have

$$i(x,y) = \int_0^{\pi} \int_{-\infty}^{\infty} I(\theta, w)|w|e^{j2\pi(x\cos\theta + y\sin\theta)w}\, dw\, d\theta \tag{15}$$

Using the Fourier slice theorem, we have

$$\begin{aligned} i(x,y) &= \int_0^{\pi} \int_{\infty}^{\infty} D_{\mathrm{p}}(\theta, w)|w|e^{j2\pi(x\cos\theta + y\sin\theta)w}\, dw\, d\theta \\ &= \int_0^{\pi} \int_{-\infty}^{\infty} d_{\mathrm{p}}(\theta, t) f(x\cos\theta + y\sin\theta - t)\, dt\, d\theta \end{aligned} \tag{16}$$

where $f(t)$ is the reconstruction filter:

$$f(t) = \int_{-\infty}^{\infty} |w|e^{j2\pi wt}\, dw \tag{17}$$

Note that $f(t)$ does not exist in an ordinary sense, but $D_{\mathrm{p}}(\theta,w)$ is essentially band-limited, and $f(t)$ can be accurately evaluated within the maximum bandwidth of $D_{\mathrm{p}}(\theta, w)$.

Geometrically, this formula performs filtered backprojection for image reconstruction. Let us decompose the formula into two parts:

$$i(x,y) = \int_0^{\pi} q(\theta, x\cos\theta + y\sin\theta)\, d\theta \tag{18}$$

where

$$\begin{aligned} q(\theta, x\cos\theta + y\sin\theta) &= \int_{-\infty}^{\infty} D_{\mathrm{p}}(\theta, w)|w|e^{j2\pi(x\cos\theta + y\sin\theta)w}\, dw \\ &= \int_{-\infty}^{\infty} d_{\mathrm{p}}(\theta, t) f(x\cos\theta + y\sin\theta - t)\, dt \end{aligned} \tag{19}$$

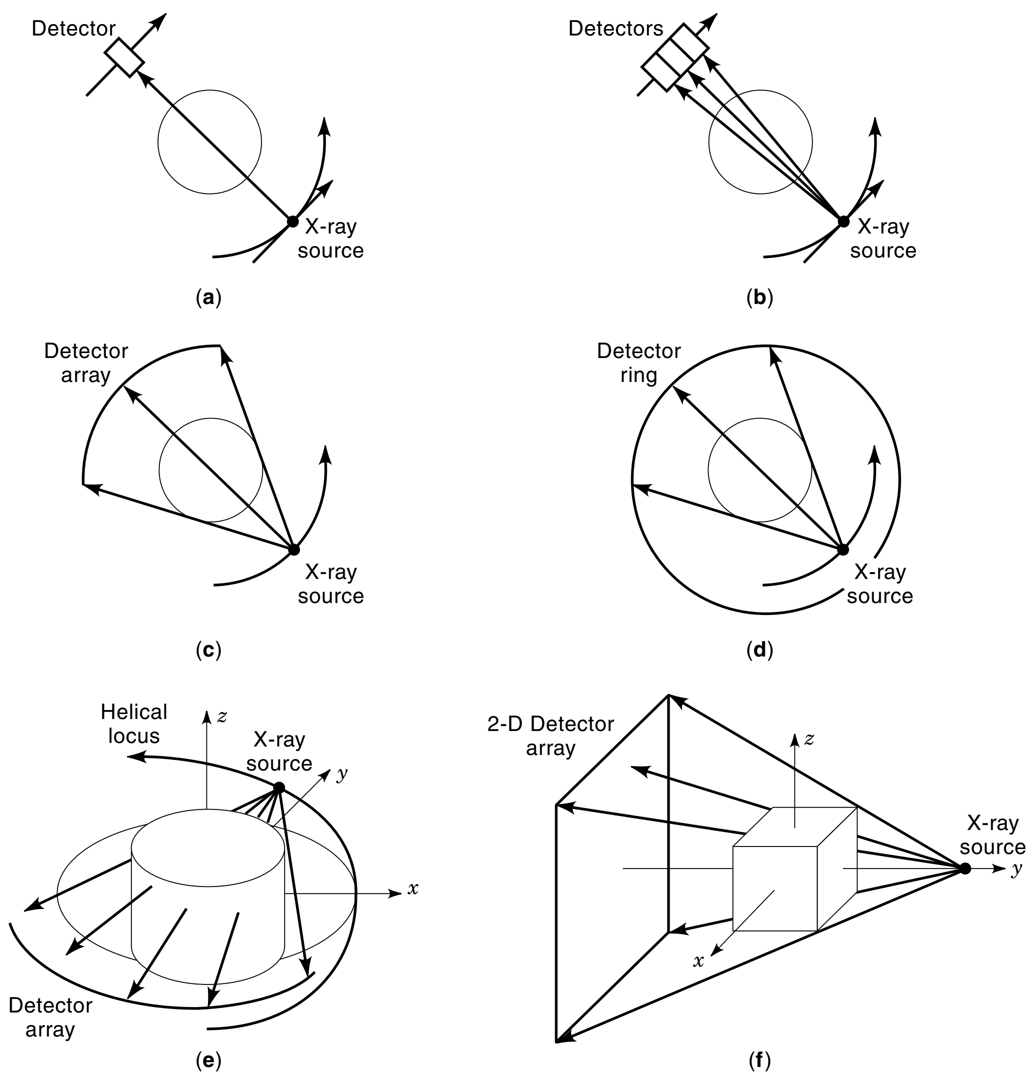

Figure 3. CT geometries. (a) First generation: one detector, translation and rotation of source and detector; (b) second generation: multiple detectors, translation and rotation of source and detectors; (c) third generation: one detector array, rotation of source and array; (d) fourth generation: one detector ring, source rotation; (e) spiral CT: simultaneous source rotation and patient translation, in either the third or fourth generation geometry; (f) cone-beam geometry: 2-D detector array.

Figure 4. Twin-beam spiral CT scanner CT-Twin. (Courtesy of Elscint, Inc.)

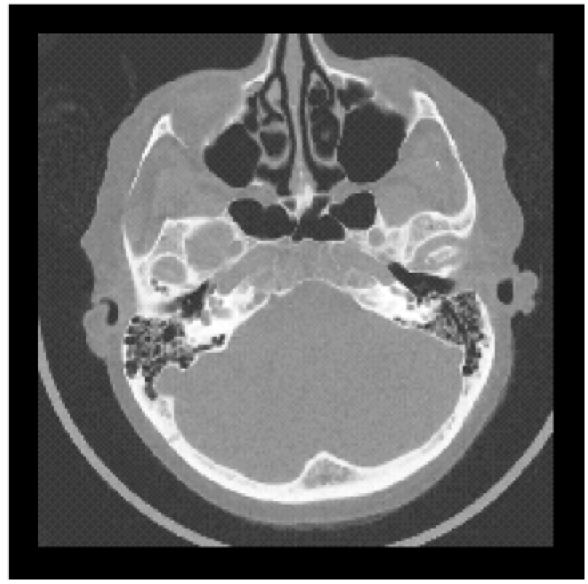

Figure 6. CT slice of a human head. (Courtesy of Picker International, Inc.)

Clearly, $q(\theta, t)$ is a filtered version of $d_p(\theta, t)$, which is the convolution of $d_p(\theta, t)$ and $f(t)$. Equivalently, $q(\theta, t)$ is the Hilbert transform of $d'_p(\theta, t)$. $i(x,y)$ is the sum of backprojected $q(\theta, t)$ along X rays. This backprojection process can be better appreciated by considering a projection at a fixed θ. In this case the X ray through a point (x,y) in the field of view intersects the projection axis at $t(x,y) = x \cos\theta + y \sin\theta$; and the filtered projection value $q(\theta, x \cos\theta + y \sin\theta)$ contributes to reconstruction of $i(x,y)$, after weighing with an appropriate angular increment. Note that the filtered projection at the angle θ will make the same contribution to reconstruction at all those points in the field of view that correspond to the same t, as shown in Fig. 8. In other words, each filtered projection is additively smeared back, or backprojected, over the field of view.

Fan-Beam Reconstruction. In fan-beam reconstruction, an X-ray point source emanates a fan-beam that penetrates an object and enters a detector array. The source and the detector array are rotated about the object to collect sufficient fan-beam projections. Fan-beam data are often described in two formats, depending upon whether a projection is sampled at equiangular or equispatial intervals. Although the algorithms for these two types of fan-beam data differ, their derivations are essentially the same. Here we focus on equispatial fan-beam reconstruction.

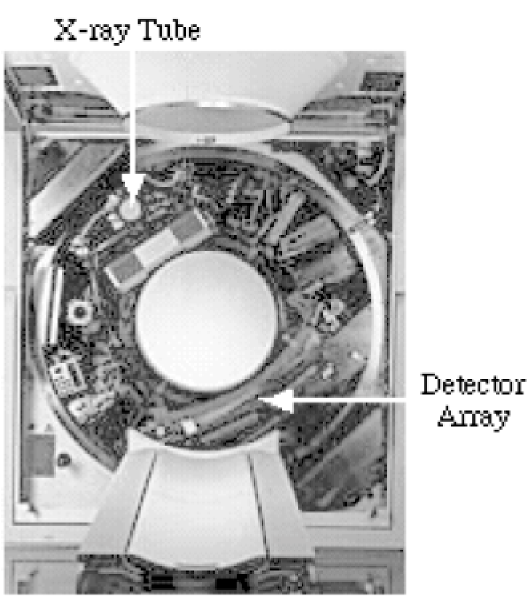

Figure 5. Inside view of a CT gantry. (Courtesy of Siemens Medical Systems.)

As shown in Fig. 9, equispatial fan-beam projections, $d_f(\beta, p)$, are generated when detectors are evenly spaced on a straight line facing the X-ray source and through the origin of the reconstruction system, where β and p are the source rotation angle and the detector position, respectively. Note that a real projection can be readily scaled onto the corresponding line through the origin. Assume that an X-ray source scanning locus $\rho(\beta)$ satisfies the following three conditions:

1. $\rho(\beta) = \rho(\beta + \pi)$.
2. $\rho'(\beta)$ exists almost everywhere.
3. $\rho^2(\beta) > \rho'(\beta)p_{\min}$ almost everywhere, $p_{\min}$ is the minimum value such that $d_f(\beta, p) = 0$, $|p| > p_{\min}$.

The third condition is easily satisfied in practice, because $\rho(\beta)$ is generally larger than $p_{\min}$ and $\rho'(\beta)$ is not very large; in particular, a circular scanning locus meets all these conditions.

With the Jacobi transform, parallel-beam data $d_p(\theta, t)$ can be converted to fan-beam data $d_f(\beta, p)$ according to the following relationship:

$$t = p\cos\gamma \quad \text{and} \quad \theta = \beta + \gamma$$

where $\gamma = \tan^{-1}[p/\rho(\beta)]$. That is,

$$t = \frac{p\rho(\beta)}{\sqrt{\rho^2(\beta) + p^2}} \quad \text{and} \quad \theta = \beta + \tan^{-1}\left(\frac{p}{\rho(\beta)}\right) \qquad (20)$$

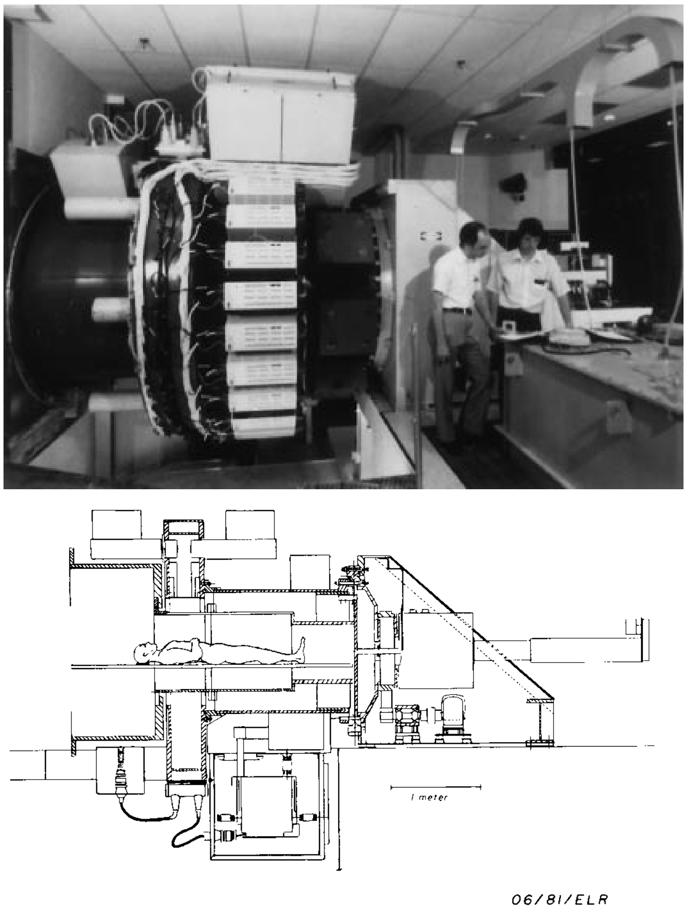

Figure 7. Dynamic spatial reconstructor (DSR). The DSR is the first system that allows near real-time tomographic imaging, and it has been applied in cardiac studies. (Courtesy of Dr. Ritman with Mayo Clinic.)

It can be verified that

$$\frac{dt\,d\theta}{dp\,d\beta} = \left| \frac{\rho^3 - p\rho\rho'}{(\rho^2 + p^2)^{3/2}} \right| \tag{21}$$

If the third condition is satisfied, we obtain

$$dt\,d\theta = \left[\frac{\rho^3}{(\rho^2 + p^2)^{3/2}} - \frac{p\rho\rho'}{(\rho^2 + p^2)^{3/2}} \right] dp\,d\beta \tag{22}$$

Then, the parallel-beam reconstruction formula can be transformed into the fan-beam reconstruction formula (12):

$$\begin{aligned} i(x,y) = \frac{1}{2} \int_0^{2\pi} \frac{\rho^2(\beta)}{[\rho(\beta) - s]^2} \int_{-\infty}^{\infty} \frac{\rho(\beta)}{\sqrt{\rho^2(\beta) + p^2}}\, d_f(\beta, p) \\ \times f\left(\frac{\rho(\beta)t}{\rho(\beta) - s} - p \right) dp\,d\beta \end{aligned} \tag{23}$$

where $t = x \cos \beta + y \sin \beta$ and $s = -x \sin \beta + y \cos \beta$. Note that the term involving ρ' is equal to zero. Similar to

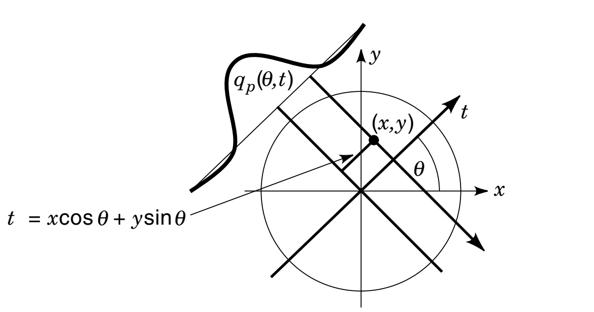

Figure 8. Backprojection of a filtered projection. After weighting with an angular increment, each filtered projection is additively smeared back to reconstruct an image.

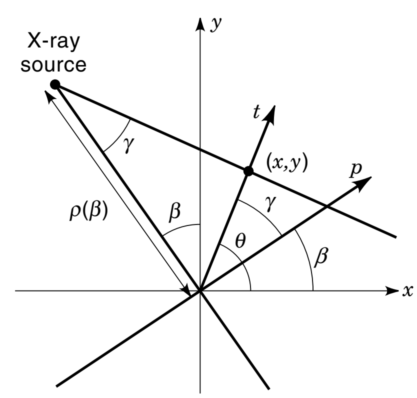

Figure 9. Geometry of equispatial fan-beam reconstruction.

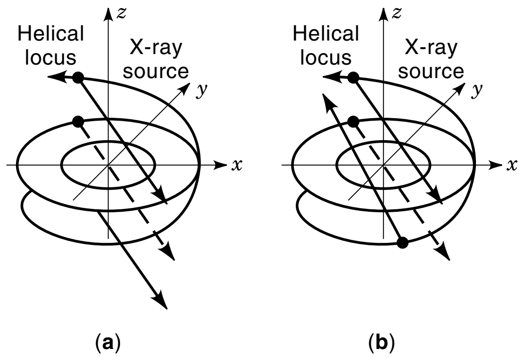

Figure 10. Spiral CT raw data interpolation. (a) Full-scan interpolation: An in-plane projection value is linearly interpolated from nearest raw data collected at the same orientation. (b) Half-scan interpolation: An in-plane projection value is linearly interpolated from nearest raw data collected at the opposite orientations.

the parallel-beam reconstruction formula, the fan-beam reconstruction formula can be interpreted as weighted filtered backprojection. If ρ is a constant, the fan-beam formula agrees with the circular fan-beam formula (13).

In spiral CT, planar projection sets are synthesized from raw projection data via interpolation. Among various interpolation methods, linear interpolation is usually preferred due to its efficiency and performance (8,14). Typical linear interpolation techniques include full-scan interpolation (FI) and half-scan interpolation (HI), as shown in Fig. 10. In the FI method, a set of planar projection data in a 360° angular range is obtained via linearly interpolating neighboring raw projection data at the same orientation; hence the involved raw data span a 720° angular range. The HI method utilizes redundancy of raw data, interpolates neighboring raw data at opposite directions, and thus reduces the angular range from 720° to 360° plus two fan-angles. Fig. 11 is a flowchart of the spiral CT process.

Exact Cone-Beam Reconstruction. When a point X-ray source and a 2-D detector array are used, cone-beam image reconstruction is required. Kirillov developed a formula for reconstruction of a complex valued n-dimensional function from complex valued cone-beam projection data (15). A sufficient condition for exact reconstruction in the Schwarz space is that an unbounded source point locus intersects almost every hyperplane. Complex-valued cone-beam formulation cannot be directly used in practice. An inversion formula in the real space was developed under the condition that almost every hyperplane through a compact function support meets a source locus transversely (16). Important theoretical analyses on cone-beam reconstruction of a real-valued function were done by Smith (17) and Grangeat (18). Due to their fundamental work, we have the following sufficient condition for exact cone-beam reconstruction: If there exists at least a cone-beam source point on any plane intersecting an object, exact cone-beam reconstruction can be achieved. Recall that if there exists at least a fan-beam source point on any straight line intersecting an object, exact fan-beam reconstruction can be achieved. Grangeat's derivation of this sufficient condition has a clearer geometrical interpretation. Various exact cone-beam reconstruction algorithms have been implemented according to Smith's theory (19–21), Grangeat's framework (22–25), and Tuy's method (26), respectively.

The Grangeat algorithm consists of two parts. In the first part, the radial derivative of planar integrals are computed, according to the relationship between the radial derivative of Radon data and the line integral of cone-beam data. The results are distributed on various spheres in the Radon space determined by a scanning locus. If the scanning locus is com-

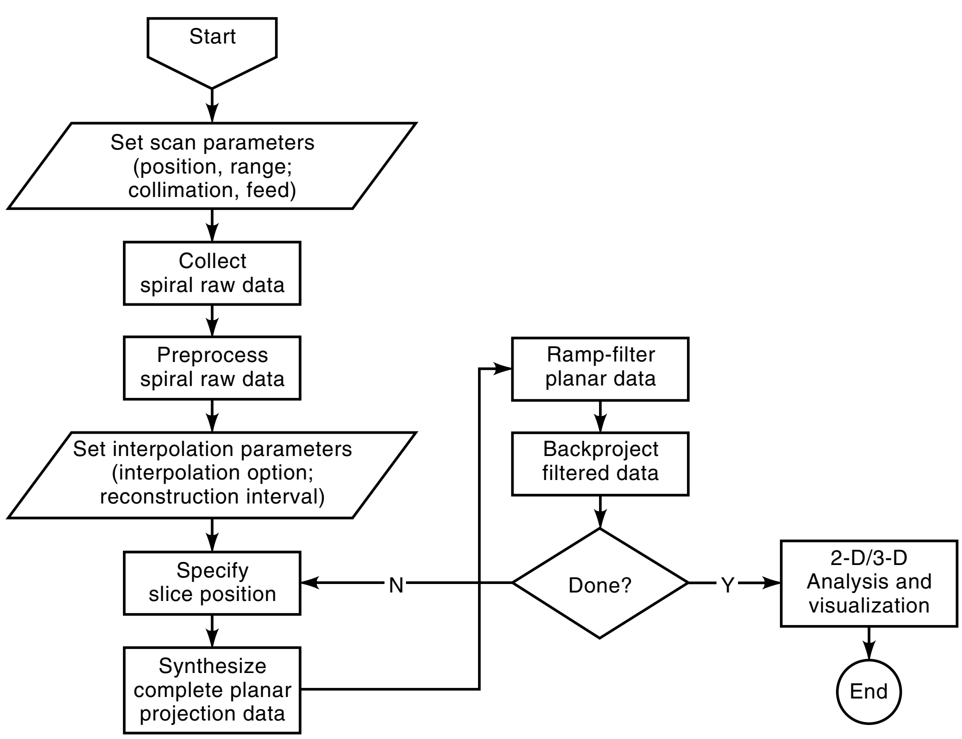

Figure 11. Flowchart of the spiral CT process.

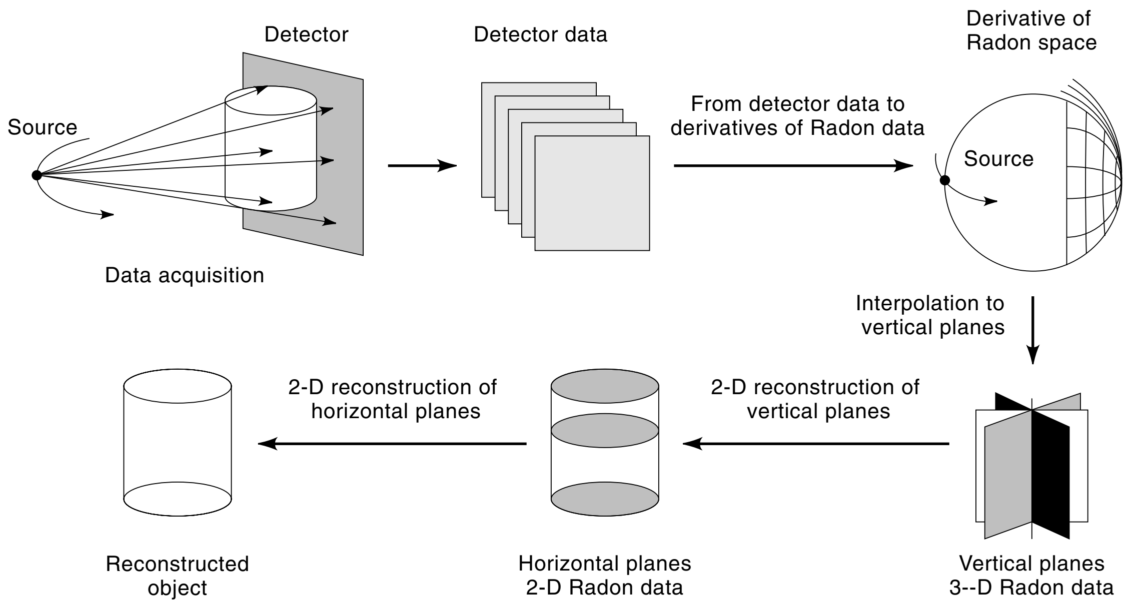

Figure 12. Exact cone-beam reconstruction. 3-D Radon data are derived from cone-beam data, interpolated on vertical planes, reconstructed into 2-D Radon data on horizontal planes, and reconstructed into an image volume. (Courtesy of Drs. Axelsson and Danielsson. Reprinted from *Phys. Med. Biol.,* **39:** 478, 1994, with permission.)

plete, the Radon space can be completely filled. In the second part, these Radon data are inverted. Although the direct filtered backprojection formula may be applied with the 3-D Radon data, the computational complexity is $O(N^5)$, where N is the size of a 3-D reconstruction grid and is proportional to the number of cone-beam projections. With the Marr method (27), the 3-D Radon inversion is decomposed into two steps, as shown in Fig. 12. First, 3-D Radon data are interpolated on vertical planes, and 2-D reconstruction is done for each vertical plane. As a result, 3-D Radon data are transformed into 2-D Radon data associated with the vertical planes. Data in the vertical planes are then grouped into data in horizontal planes, and 2-D reconstruction is performed for each horizontal plane. This method has a computational complexity of $O(N^4)$.

Axelsson and Danielsson developed a direct Fourier method (24), which is a refined version of the Grangeat algorithm. Among existing algorithms, the Axelsson and Danielsson algorithm is computationally most efficient for a sufficiently large amount of data and has a complexity of $O(N^3 \log N)$ (24). The reduction was made by adapting the linogram method (28). The linogram method requires that the projection profile sampling step and the projection angular increment vary appropriately, so that equidistant samples along concentric squares can be formed in the Fourier domain, and reconstruction accelerated. Exact filtered backprojection algorithms for cone-beam reconstruction were independently derived by Defrise and Clack (22) and by Kudo and Saito (23), which require that a scanning locus be complete, data redundancy weighting and nonstationary 2-D filtering be applied.

Approximate Cone-Beam Reconstruction. Despite progress in exact cone-beam reconstruction, approximate cone-beam reconstruction remains important, especially in the cases of incomplete scanning loci and partial detection coverage. Furthermore, approximate reconstruction is usually associated with higher computational efficiency and may produce less image noise and ringing. We focus on Feldkamp-type cone-beam reconstruction, the main stream of approximate cone-beam reconstruction.

Let $i(x, y, z)$ be an image with a cylindrical support. A scanning locus is described in a cylindrical coordinate system $(\rho(\beta), h(\beta), \beta)$, where β is the source rotation angle around the z axis, without loss of generality $\beta \in [0, 2\pi)$, $\rho(\beta)$ describes the distance between the source and the z axis, and $h(\beta)$ is the distance from the source to the x–y plane. If the 3-D scanning locus is vertically projected onto the x–y plane, a 2-D scanning locus will be obtained. We assume that this 2-D scanning locus meets all the three fan-beam scanning conditions described earlier. An equispatial cone-beam projection is denoted as $d_c(\beta, p, \zeta)$, where the ζ axis of the detection plate p-ζ is superimposed on the z axis, and the central normal of the detection plate is toward the x-ray source.

In Fig. 13, we consider reconstruction of a point object $\delta(x - x_0, y - y_0, z - z_0)$ from its cone-beam data, which can be expressed as

$$d_{c,\delta}(\beta, p, \zeta) = \left[\frac{\rho^2(\beta)}{\sigma^2(\beta)}\right]\left[\frac{\sqrt{\rho^2(\beta) + p^2 + \zeta^2}}{\rho(\beta)}\right]\delta(p - p_0)\delta(\zeta - \zeta_0) \tag{24}$$

where $\sigma(\beta)$ is the difference between $\rho(\beta)$ and the signed distance from the point object to the detection plate, and (p_0, ζ_0) are coordinates of the point object projected on the detection plate. Geometrically, the first factor scales the point object because of the divergence of the cone beam, and the second factor is due to the angle between the X ray through (x_0, y_0, z_0) and the normal of the p-ζ plate. We note that in the plane $z = z_0$, the equispatial fan-beam projection of the point object

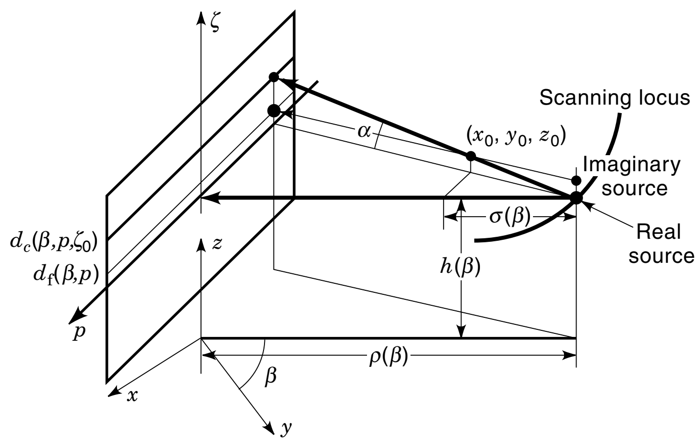

Figure 13. Approximate cone-beam reconstruction. Cone-beam data are corrected to fan-beam data by multiplying cone-beam data with the cosine of the corresponding X-ray tilting angle. For a point object, the corrected fan-beam data are exact.

is

$$d_{\mathrm{f},\delta}(\beta, p) = \left[\frac{\rho^2(\beta)}{\sigma^2(\beta)}\right]\left[\frac{\sqrt{\rho^2(\beta)+p^2}}{\rho(\beta)}\right]\delta(p-p_0)\delta(0) \qquad (25)$$

Comparing Eq. (24) with Eq. (25), we observe that the fan-beam projection $d_{\mathrm{f},\delta}(\beta, p)$ of this point object can be exactly obtained by multiplying the corresponding horizontal profile $d_{c,\delta}(\beta, p, \zeta_0)$ of the cone-beam projection with the cosine of the X-ray tilting angle; mathematically,

$$d_{\mathrm{f},\delta}(\beta, p) = \frac{\sqrt{\rho^2(\beta)+p^2}}{\sqrt{\rho^2(\beta)+p^2+\zeta_0^2}}\, d_{c,\delta}(\beta, p, \zeta_0) \qquad (26)$$

Clearly, applying the fan-beam reconstruction formula derived in the preceding subsection with corrected cone-beam data, exact reconstruction can be achieved in the plane $z = z_0$.

Generally speaking, $i(x, y, z)$ is not a point object, but it can be viewed as a combination of many point objects. To reconstruct a point object at (x, y, z), we can correct cone-beam data in the same way to obtain approximate fan-beam data, and then perform fan-beam reconstruction. By doing so, we immediately obtain the generalized Feldkamp cone-beam reconstruction formula (29):

$$i(x,y,z) = \frac{1}{2}\int_0^{2\pi}\frac{\rho^2(\beta)}{(\rho(\beta)-s)^2}\int_{-\infty}^{\infty}\frac{\rho(\beta)}{\sqrt{\rho^2(\beta)+p^2+\zeta^2}} \times d_c(\beta,p,\zeta) f\left(\frac{\rho(\beta)t}{\rho(\beta)-s}-p\right) dp\, d\beta \qquad (27)$$

where $t = x \cos\beta + y \sin\beta$, $s = -x \sin\beta + y \cos\beta$, and $\zeta = \rho(\beta)(z - h(\beta))/[\rho(\beta) - s]$. Fig. 14 shows a real cone-beam projection of a snail as well as a surface-rendered image reconstructed using the generalized Feldkamp algorithm with the X-ray cone-beam micro-CT system at the AMIL, SUNY/Buffalo. Because this formula is based on fan-beam reconstruction, it is also in a weighted filtered backprojection format.

With a circular scanning locus, the generalized Feldkamp cone-beam formula is equivalent to the well-known Feldkamp formula (30). The generalized Feldkamp formula allows a wide class of scanning loci, reconstructs spherical, rod-shaped and planar specimens, and preserves all the exactness properties Feldkamp et al. established (30), including that the longitudinal integral of a reconstructed volumetric image is equal to that of the actual image.

Interestingly, the generalized Feldkamp reconstruction can be similarly formulated in a rotated reconstruction system x'–y'–z' after cone-beam data are corrected onto the new imaginary detector plane through the z' axis. Suppose that the vertical projection of a 3-D scanning locus allows exact fan-beam reconstruction, it can be proven in the same way that the integral of a reconstructed volumetric image along the z' axis is exact. Note that if the projected scanning locus does not satisfy the three fan-beam scanning conditions, Feldkamp-type reconstruction can still be performed using an appropriate fan-beam reconstruction formula (data rebinning may be involved).

The exact longitudinal integral of a reconstructed volumetric image equals the 2-D parallel-beam projection along the direction of integration. Therefore, exact stereoimaging from incomplete cone-beam data is feasible. If a sufficient amount of exact 2-D parallel projection data is available, exact 3-D image reconstruction can be performed. Therefore, a sufficient condition for exact cone-beam reconstruction can be stated below: If for any projection direction a projected scanning locus

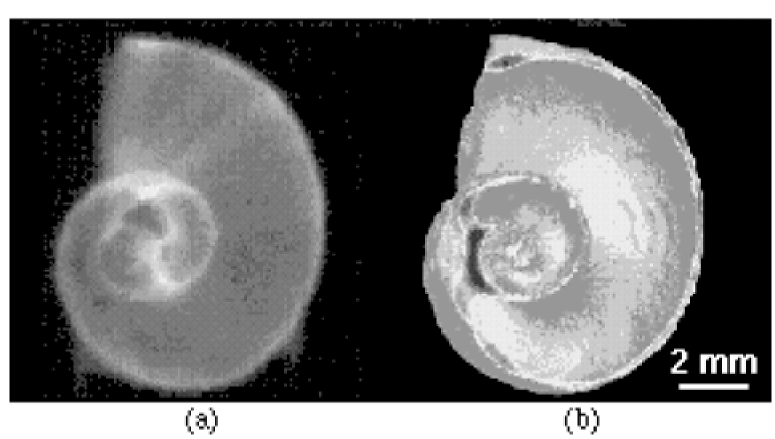

Figure 14. Cone-beam X-ray microtomography. (a) Cone-beam projection. (b) Surface rendered view of a snail shell reconstructed using the generalized Feldkamp algorithm. (Courtesy of Dr. P. C. Cheng, S. J. Pan, A. Shih, and W. S. Liu with AMIL, SUNY/Buffalo.)

is complete for exact fan-beam reconstruction on a projected object support, the object can be exactly reconstructed. This stereoimaging based sufficient condition is equivalent to the traditional sufficient condition. If the stereoimaging-based sufficient condition is satisfied, for any projection direction the projected scanning locus is complete, and we have the family of all the planes parallel to the projection direction and containing at least one source position. That is, the traditional sufficient condition is also satisfied. If the stereoimaging-based sufficient condition is not satisfied, there is a projection direction along which the projected scanning locus is incomplete, a line can be found that intersects the projected object support but meets no projected source point, and this line represents a plane that intersects the object but contains no source point. That is, the traditional sufficient condition is violated.

Iterative Reconstruction

Available noniterative cone-beam algorithms require that projections should not be truncated along at least one direction. Therefore, satisfactory cone-beam reconstruction with these algorithms is impossible in cases where objects contain X-ray opaque components and/or are larger than the cone-beam aperture defined by effective detection area and X-ray source position. Various iterative methods are known for years. Recently, Snyder et al. interpreted the expectation maximization (EM) formula for emission CT (31) in a deterministic sense, and established its properties on convergence and optimality (32).

Using the notation of Snyder et al. (32), the linear, discrete, and nonnegative deblurring problem is formulated as inversion of

$$\sum_{\vec{x}\in\mathbf{X}} h(\vec{y}|\vec{x})c(\vec{x}) = a(\vec{y}) \tag{28}$$

where $a(\vec{y})$ is an observed function, $h(\vec{y}|\vec{x})$, a known blurring kernel, $c(\vec{x})$ a function to be recovered, $\vec{x} \in \mathbf{X}$, $\vec{y} \in \mathbf{Y}$, and all the functions are nonnegative. The following iterative deblurring formula can be used:

$$c_{k+1}(\vec{x}) = c_k(\vec{x})\frac{1}{H_0(\vec{x})}\sum_{\vec{y}\in\mathbf{Y}}\left[\frac{h(\vec{y}|\vec{x})}{\sum_{\vec{x}'\in\mathbf{X}} h(\vec{y}|\vec{x}')c_k(\vec{x}')}\right]a(\vec{y}) \tag{29}$$

where $H_0(\vec{x}) = \sum_{\vec{y}\in\mathbf{Y}} h(\vec{y}|\vec{x})$, $c_k(\vec{x})$ and $c_{k+1}(\vec{x})$ are current and updated guesses of $c(\vec{x})$. It was shown that $\sum_{\vec{x}\in\mathbf{X}} h(\vec{y}|\vec{x})c_\infty(\vec{x})$ fits $a(\vec{y})$ nonnegatively, monotonically, and optimally in the sense of the I-divergence $I(a\|b)$ (32)

$$I(a\|b) = \sum_{\vec{y}\in\mathbf{Y}} a(\vec{y})\log\frac{a(\vec{y})}{b(\vec{y})} - \sum_{\vec{y}\in\mathbf{Y}}[a(\vec{y}) - b(\vec{y})] \tag{30}$$

Use of the I-divergence to define the optimality is justifiable (33,34). Briefly, among many discrepancy measures, the I-divergence and the Euclidean distance were shown to be appropriate choices in nonnegative and real spaces, respectively.

In their work (32), Snyder et al. require a strictly positive kernel, $h(\vec{y}|\vec{x}) > 0$. Recently, this constraint was relaxed to allow a nonnegative kernel, $h(\vec{y}|\vec{x}) \geq 0$, under the following extended assumptions (35):

1. $a(\vec{y}) > 0$ for all $\vec{y}$,
2. $a(\vec{y})$ is summable,
3. $H_0(\vec{x}) = \sum_{\vec{y}\in Y} h(\vec{y}|\vec{x}) > 0$,
4. $H_0(\vec{y}) = \sum_{\vec{x}\in X} h(\vec{y}|\vec{x}) > 0$,
5. $h(\vec{y}|\vec{x}) \geq 0$ for all $\vec{x}$, $\vec{y}$,
6. $h(\vec{y}|\vec{x})$ is summable with respect to $\vec{x}$ and $\vec{y}$.

Several comments on the extended assumptions are in order. First, $a(\vec{y}) > 0$ may appear more restrictive than the original $a(\vec{y}) \geq 0$, but it is not. Actually, a deblurring problem with $a(\vec{y}) \geq 0$ can be transformed to the one with $a(\vec{y}) > 0$ by the following preconditioning procedure: if $a(\vec{y}_0) = 0$, $c(\vec{x})$ is set to zero for all $\vec{x} \in X(\vec{y}_0)$, where $X(\vec{y}_0)$, $= \{\vec{x} \in X, h(\vec{y}_0|\vec{x}) \neq 0\}$, then $\vec{y}_0$ and $X(\vec{y}_0)$ can be removed from Y and X, respectively. This is consistent with what was done by Snyder et al.: if $a(\vec{y}) \equiv 0$, then $c(\vec{x}) \equiv 0$ (32). Also, $H(\vec{x}) > 0$ means that $c(\vec{x})$ is somehow measured at any specific $\vec{x}$. If $H(\vec{x}_0) = 0$, $c(\vec{x}_0)$ is totally unobservable. Hence, $\vec{x}_0$ can be removed from X. On the other hand, $H(\vec{y}) > 0$ means that every $a(\vec{y})$ carries a certain amount of information about $c(\vec{x})$. Actually, if $H(\vec{y}_0) = 0$, $h(\vec{y}_0|\vec{x}) = 0$ for all $\vec{x}$, and no information about $c(\vec{x})$ can be derived from $a(\vec{y}_0) \equiv 0$. Therefore, $\vec{y}_0$ can be removed from Y. These preconditioning operations exclude uninformative situations. We showed that all the properties Snyder et al. established remain essentially valid under the extended assumptions [mainly, $h(\vec{y}|\vec{x}) \geq 0$, instead of $h(\vec{y}|\vec{x}) > 0$].

Although it is computationally expensive, the major advantages of the iterative approach include insensitivity to data noise and capability of reconstructing an optimal image in the case of incomplete data, where traditional Fourier-transform-based methods are subject to serious artifacts. With rapid evolution of computing technologies, iterative reconstruction will be more practical.

Theoretically, a projection datum is the value of a linear integral along an X-ray path contained in an object. After discretization of detection and reconstruction systems, continuous projection can be approximated as values at a detection grid, each of which equals a sum of weighted values of those voxels that are in a neighborhood of the correponding X ray. Then, the generic iterative deblurring formula can be specialized for image reconstruction in parallel-beam, fan-beam, or cone-bean geometry.

A flowchart of the iterative cone-beam reconstruction algorithm is given in Fig. 15. First, cone-beam projection data are measured given a cone-beam geometry and a scanning locus. Based on measured cone-beam data, a characteristic projection mask is formed to indicate whether or not a reading is significant for a combination of source and detector positions. For example, if there are X-ray opaque structures in an object, some detectors may receive little photons, and corresponding data are lost. To take beam divergence and data incompleteness into account, a relaxation function (the discrete version of $H_0(\vec{x}_p)$) is generated from the projection mask, the cone-beam geometry, and the scanning locus. Also, a positive intermediate image volume is initialized. In each iteration, cone-beam projection data are estimated via ray-tracing based on the intermediate image volume. Discrepancies between measured and estimated projection data are computed as ratios for every significant combination of detector and source positions. Then, these ratios are backprojected over the 3-D image grid, multiplied with the intermediate image, and

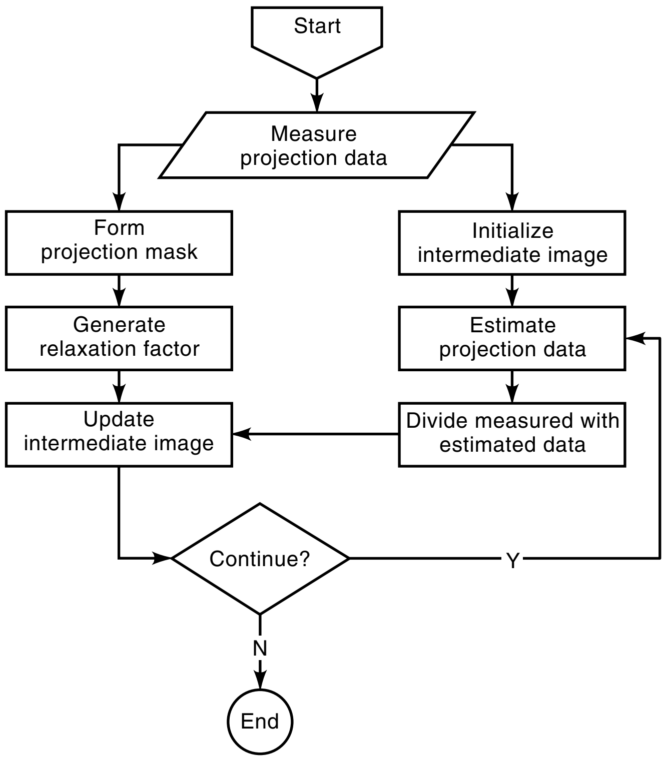

Figure 15. Flowchart of the EM-type iterative X-ray cone-beam CT algorithm with data incomplete due to either X-ray opaque structures or an insufficient cone-beam aperture.

divided by the relaxation factor to obtain an updated image. A priori knowledge, such as a known image support, can be enforced upon the updated image. Image quality and fitting errors may be estimated after each iteration. A numerically simulated example is presented in Fig. 16.

Iterative deblurring has been used for PET and SPECT image reconstruction, where it is interpreted in a statistical sense for maximization of the likelihood. The iterative X-ray CT algorithm has two important features. First, this algorithm is interpreted in a deterministic sense, which minimizes the I-divergence of measured and fitted data instead of maximizing the likelihood of the solution. Actually, the likelihood in X-ray CT can be maximized using a more complicated iterative formula (31). Second, it handles data incompleteness in a unified way due to introduction of the projection mask. Consequently, the iterative X-ray CT algorithm is a powerful framework for metal artifact reduction and local region reconstruction from truncated data.

IMAGE QUALITY

Image quality can be described in two categories: resolution and artifacts. Image resolution has three aspects: high-contrast resolution (spatial resolution) for distinguishing adjacent objects of high-contrast, low-contrast resolution (contrast resolution) for differentiating an object from its background which is similar to the object in gray-scale, and temporal resolution for resolving time-varying structures. Image noise imposes a grainy appearance due to random fluctuations of the X-ray photon flux, and it is a major factor in defining low-contrast resolution. Image artifacts are structured or patterned interference over the field of view. Although the X-ray dosage delivered to the patient is an extremely important issue in medical CT and closely related to image quality, it is beyond the scope of this article. Interested readers are referred to Rothenberg and Pentlow (36) and McGhee and Humphreys (37). In discussion of image quality, we emphasize unique features of spinal CT, the standard mode of medical X-ray CT.

Resolution

Spiral CT was introduced for faster volumetric scanning than conventional incremental CT. However, spiral CT produces inconsistent projection data for any transaxial plane, and it broadens the slice sensitivity profile (SSP) as compared with conventional CT. It appeared that temporal resolution of spiral CT was improved at the cost of degraded high- and low-contrast resolution. However, as will be seen below, this is not necessarily the case.

High-Contrast Resolution. Generally, high-contrast resolution in a scanning plane can be easily visualized using the multibar phantom, as shown in Fig. 17, which is an array of high-contrast bars being uniform in both the bar width and their separation. When the width and separation of the bars become smaller, the image contrast of the bars will decrease. The in-plane resolution is described by the modulation transfer function (MTF), which is the ratio between the image con-

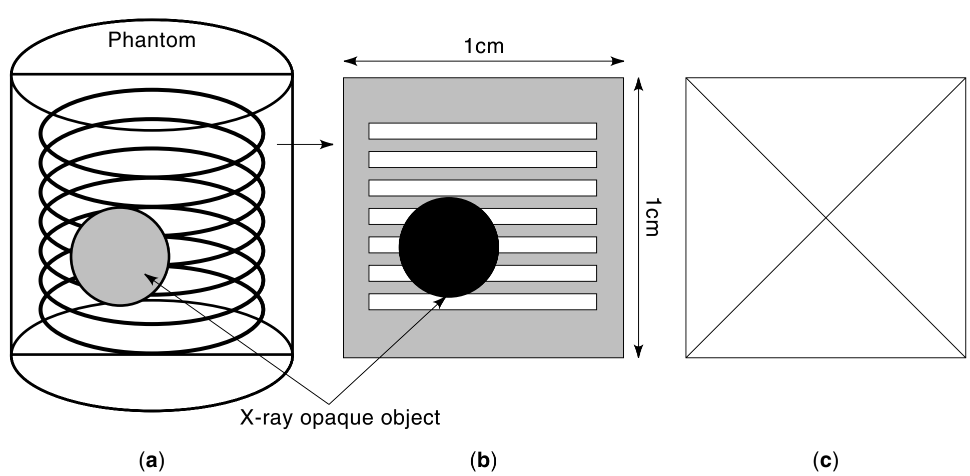

Figure 16. Numerical simulation of EM-type iterative X-ray cone-beam tomography with a cylindrical phantom from incomplete data due to an embedded X-ray opaque sphere. (a) Diagram of the phantom containing 7 disks (thickness not shown) and the opaque sphere, (b) middle sagittal slice, (c) reconstructed counterpart after 40 iterations.

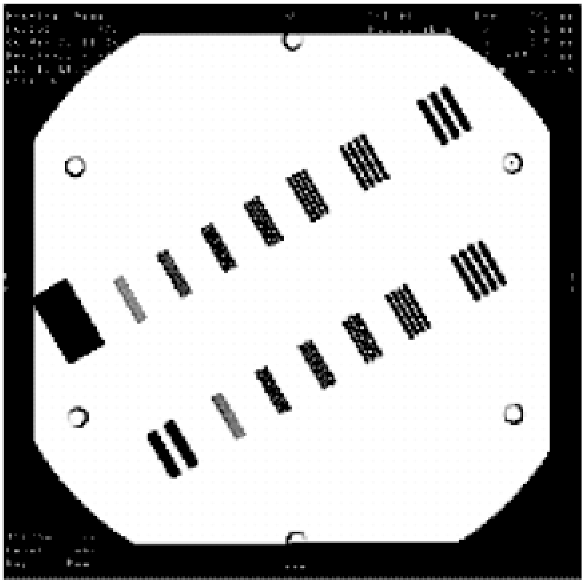

Figure 17. High-contrast resolution is measured with the multibar phantom. The modulation transfer function is described by the ratio between the image contrast and the bar contrast as a function of the spatial frequency of the bars. (Courtesy of Picker International, Inc.)

trast and the object contrast as a function of the spatial frequency of the bars. Ideally, the MTF is defined in terms of sinusoidal functions, which are, however, difficult to fabricate. On the other hand, high-contrast resolution through the scanning plane is described in terms of the SSP, which can be computed as the derivative of an edge response in a plane orthogonal to the scanning plane.

Several studies have shown that in-plane high-contrast resolution of spiral CT is quite similar to that of incremental CT (8,14). As far as through-plane high-contrast resolution is concerned, although spiral CT degrades the SSP, it allows retrospective reconstruction: Raw data are collected first, and any transaxial slice can be reconstructed afterward; in other words, the longitudinal sampling rate in spiral CT can be much higher. To compare through-plane high-contrast resolution, the SSPs and corresponding MTFs were derived for incremental CT and spiral CT with the HI method (38). The one-tenth-cutoff and mean-square-root measures were used to quantify the bandwidths of the MTFs. It was proven that for a given X-ray dose, spiral CT with overlapping reconstruction has a wider bandwidth and thus better longitudinal high-contrast resolution than incremental CT. It is recommended that 3–5 slices be reconstructed per slice thickness. Experiments also demonstrated merits of overlapping reconstruction in spiral CT (39). With state-of-the-art spiral CT scanners, volumetric images of sub-mm isotropic 3-D resolution can be obtained.

Low-Contrast Resolution. Low-contrast resolution characterizes recognizability of a low-contrast object and is influenced by several factors, including the object size, contrast between object and background, image noise, and the system MTF. Image noise is primarily determined by the dose setting of the X-ray tube, the slice thickness, the reconstruction algorithm, the characteristics of the CT scanner, and the structures scanned in the field of view. As shown in Fig. 18, low-contrast resolution can be measured with a multihole phantom. A good descriptor of low-contrast resolution is the CT value difference of those holes that are barely recognizable in the image.

Conventional CT being the standard, spiral CT with the HI method increases image noise, while spiral CT with the FI method decreases image noise (8,14,40). On the other hand, the HI method degrades the SSP significantly less than the FI method (8,14). As a result, spiral CT could suffer from either poorer high-contrast resolution using the FI method or poorer low-contrast resolution using the HI method. Because both the HI and FI methods have their advantages and disadvantages, they can be combined for a balance. Specifically, from a spiral CT raw data set and at a given longitudinal position, two transaxial images can be reconstructed using the FI and HI methods, respectively. Then, the two images are averaged to produce a new image. Apparently, the averaging operation can be moved into the interpolation process for better efficiency, resulting a balanced interpolation method. The image noise, the one-tenth-cutoff, and the mean-square-root measures of the longitudinal MTFs were derived for incremental CT and spiral CT using this balanced interpolation method and were experimentally verified (41). It was found that given an X-ray dose and a longitudinal bandwidth, spiral CT on average allows less image noise and better low-contrast resolution than incremental CT.

Temporal Resolution. To capture rapidly varying structures, the speed of data acquisition is critical. The development of CT scanners was motivated, to a major degree, by the need for better temporal resolution. The primary indicator of temporal resolution is the period of data acquisition, although the temporal resolution also depends on the reconstruction algorithm. State-of-the-art spiral CT scanners collect projection data of 360° in a second. Recently, CT fluoroscopy (CTF) has attracted increasing interest. In CTF, a patient is contin-

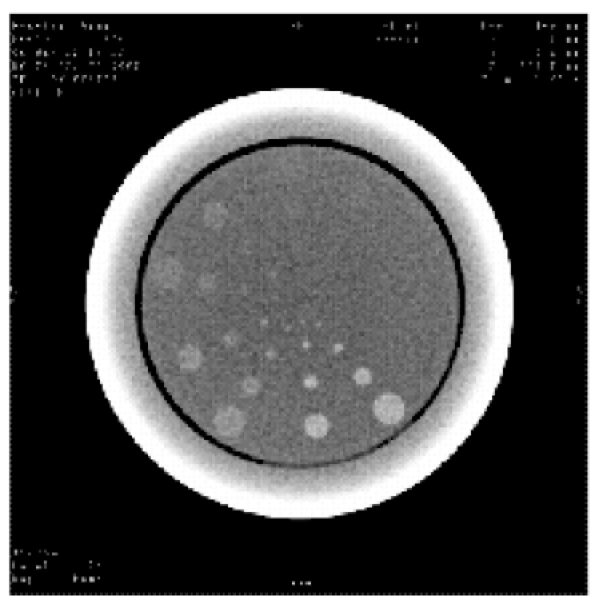

Figure 18. Low-contrast resolution is measured with a multi-hole phantom. (Courtesy of Picker International, Inc.)

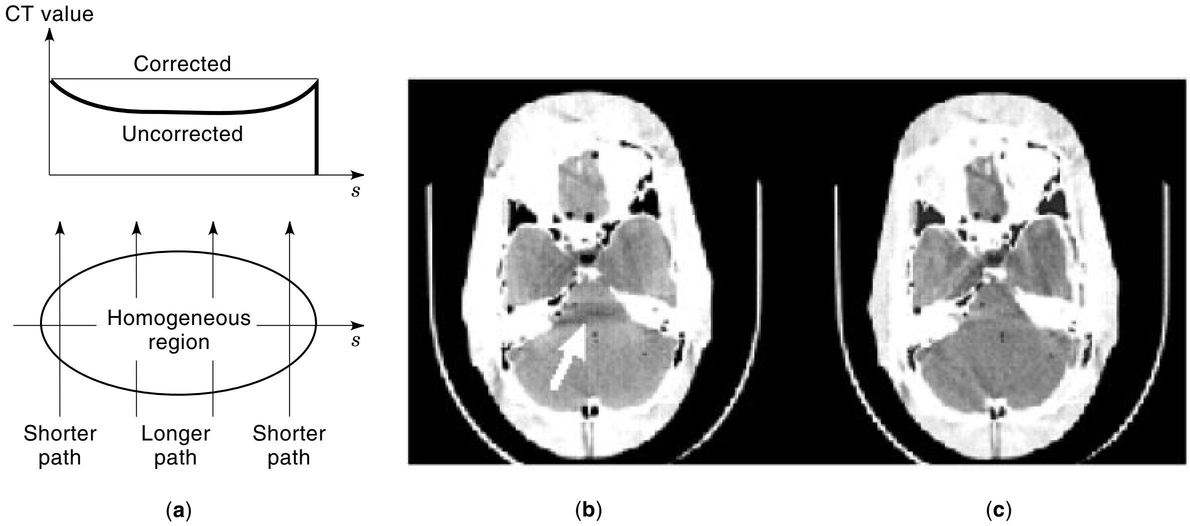

Figure 19. Beam-hardening artifacts and correction. (a) Uncorrected "cupping" profile of a homogeneous phantom due to beam hardening, which causes a right shift in the effective energy of the X-ray beam over longer paths. (b) Image reconstructed at the petrous bones without beam-hardening correction, in which an erroneous shadow is indicated by the arrow. (c) With beam-hardening correction. (Courtesy of Dr. Jiang Hsieh at GE Medical Systems.)

uously scanned while an intervention is done such as a needle being inserted. Recently, Hsieh (42) quantified temporal resolution of CTF in terms of the time lag and the time delay. The time lag is the minimum time needed to reveal the actual movement of the biopsy needle, while the time delay is the minimum time for the needle to reach its real location in the CT image. The DSR and the electron-beam CT scanner reduce the scanning time by an order of magnitude to about one-tenth second. Generally, the power of an X-ray source can be a limiting factor. The faster the scanning is, the less the dose delivered, and the more the image noise. A trade-off between temporal resolution and low-contrast resolution depends upon the intended application of CT images.

Artifacts

Substantial research has been done on causes, characteristics, and correction of image artifacts (43). We only discuss the most common artifacts: beam hardening artifacts, blurring artifacts, motion artifacts, metal artifacts, and stair-step artifacts.

Beam-Hardening Artifacts. Conventional X-ray sources for medical CT are rotating anode tubes, which have polychromatic spectra. That is, X-ray photons emitted from a X-ray tube do not all have the same energy. The X-ray attenuation of an object depends on the photon energy. As an X-ray beam traverses an object, the higher energy portion of the X-ray spectrum increases, since lower energy photons are attenuated more. If this nonlinear beam-hardening effect is not compensated, a "cupping" in image gray-scale will be seen. The beam-hardening artifacts are more serious when high X-ray absorption structures are in the field of view. Means for suppressing beam-hardening artifacts include prefiltering X-rays, avoiding high X-ray absorbing regions if possible, and applying appropriate algorithms (44,45). Figure 19 illustrates beam-hardening artifacts and correction with a homogeneous phantom and an image at the petrous bones, respectively. Scattered radiation-induced artifacts should also be mentioned, which lead to cupping, streaks, and CT number errors. It was shown that this type of artifact can be more significant than beam-hardening artifacts for large body parts, such as in the pelvis, and may be corrected to a substantial degree, assuming a constant scatter background (46).

Blurring Artifacts. Blurring artifacts refer to a blurred appearance of discrete structures in a CT image, due mainly to sizes of an X-ray source and detectors. Another name for this type of artifact is partial volume averaging, since a reconstructed voxel value is approximately an average of attenuation distribution in a neighborhood of the center of that voxel. A common phenomenon is that sharp edges look blurred in an image, indicating a degraded system high-frequency response. The blurring artifacts are certainly undesirable when details are examined. For example, blurring in spiral CT images limits the in vivo study on the middle and inner ear for cochlear implantation.

Digital deblurring is an established approach to undo image blurring retrospectively. There are various image deblurring algorithms available. It was demonstrated that the iterative maximum likelihood deblurring method produced a satisfactory deblurring effect in spiral CT (35,47). The spiral CT imaging process can be approximated as a 3-D linear spatially invariant system, and the 3-D system point spread function (PSF) modeled as a separable Gaussian function (35). Roughly speaking, in iterative deblurring of a reconstructed image, a previous guess is convolved with the system PSF, the reconstructed image is point by point divided by the convolved guess, the ratio image is convolved again with the PSF, and the convolved ratio image is point by point multiplied by the previous guess to update it. The reconstructed image can be used as an initial guess. This iterative deblurring method is a special case of the linear, discrete, and

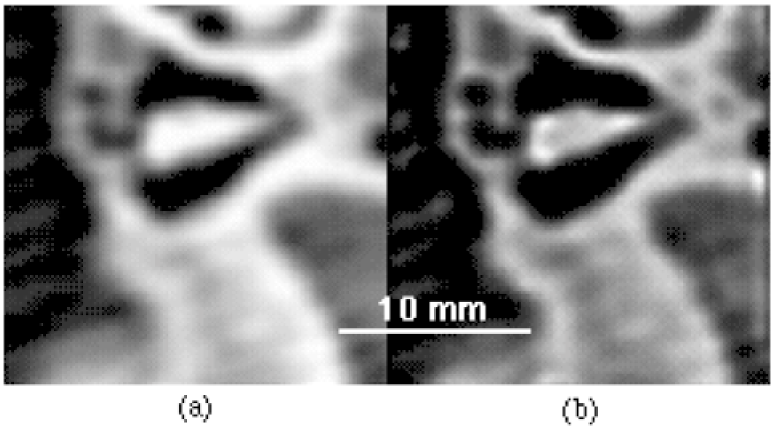

Figure 20. Blurring artifacts and correction. (a) Spiral CT slice of the temporal bone. (b) Counterpart deblurred using the iterative maximum likelihood algorithm. (Original data courtesy of Dr. Gregory Esselman with Washington University.)

nonnegative deblurring formula described earlier, and can be regularized for suppression of deblurring artifacts, which are primarily image noise and edge ringing (35). Figure 20 shows a spiral CT slice of temporal bone and the counterpart iteratively deblurred.

Motion Artifacts. Motion artifacts are produced in a CT image if an object is not static but assumed so in the reconstruction process. In medical CT, anatomical structures move periodically due to respiration or cardiac pulsation. Severely injured patients or children frequently move during scanning. Fig. 21 demonstrates that respiratory motion artifacts can be significant with incremental CT and can be eliminated by spiral CT single breath-hold scanning. Crawford et al. (48) developed a pixel-specific filtered backprojection algorithm for motion artifact reduction. In their algorithm, in-plane motion is corrected by pixel-specific reconstruction in the coordinate system associated with the in-plane motion.

Metal Artifacts. Metal artifacts are typically pronounced dark and bright streaks around a metal part in an image reconstructed via filtered backprojection, as shown in Fig. 22. Because of the higher atomic number, the metal attenuates X-rays in the diagnostic energy range much more than soft tissues and bone. As a result, almost no photons penetrate the metal, and corresponding line integrals are lost. As mentioned earlier, metal artifacts can be optimally suppressed via iterative deblurring in the sense of the *I*-divergence (49).

Stairstep Artifacts. Stairstep artifacts are well known in conventional CT, and have special features in spiral CT (50). They are associated with inclined surfaces in reformatted longitudinal slices, as shown in Fig. 23. In spiral CT, the stairstep artifacts were due to not only large reconstruction interval but also asymmetric spiral CT interpolation. Even if the reconstruction interval is sufficiently small, the stairstep artifacts will appear as long as the object cross section varies longitudinally. In this case, the height of the stairsteps depends on the pattern of asymmetry in the transverse image, which is mainly determined by the interpolation method and the structures in the field of view. For minimal stairstep artifacts, both detector collimation and table increment should be minimized, which should be less than the longitudinal dimension of features of interest if it is possible.

DISCUSSION AND FURTHER READINGS

Although X-ray CT has been intensively studied for years, further developments are anticipated. Most important, spiral CT remains an active area. Spiral CT involves more parameters and raw data processing than conventional CT. Optimi-

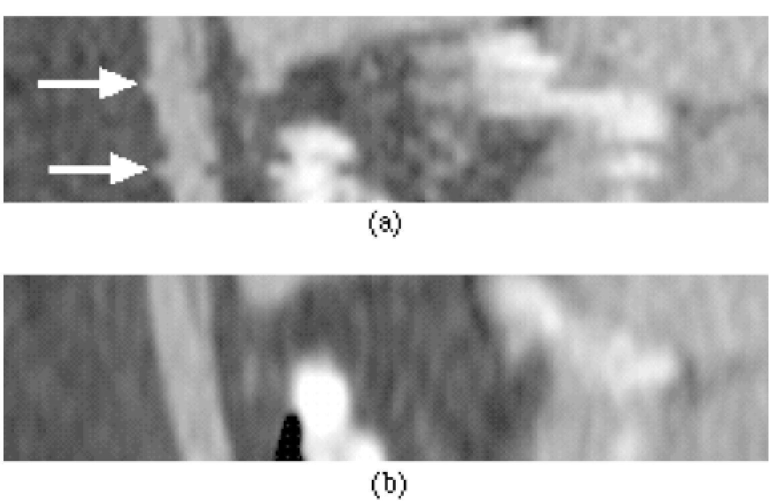

Figure 21. Respiratory motion artifacts. (a) Artifacts in multiplanar reformation with incremental CT (85 s), as indicated by arrows, and (b) eliminated with single breath-hold spiral CT scanning (12 s). (Courtesy of Dr. James Brink, Yale University.)

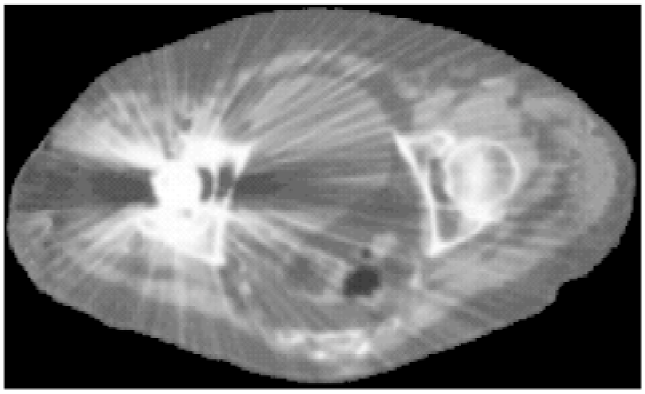

Figure 22. Metal artifacts caused by a prosthesis. (Courtesy of Dr. Douglas Robertson, Washington University.)

zation of imaging protocols and image quality needs major additional efforts (51). Multislice spiral CT is emerging for faster scanning and wider coverage. Cone-beam spiral CT seems a promising mode in medical imaging, industrial inspection, airport screening, and other applications. It is desirable and possible that an exact cone-beam spiral CT algorithm could be designed that takes longitudinally truncated cone-beam data and can be efficiently implemented.

The wavelet approach has a significant potential for radiation reduction and multiresolution reconstruction. Olson and DeStefano (52) observed that space-frequency localized wavelet bases can be used in sampling the Radon transform and performing local region reconstruction. Zhao et al. (53) established an upper error bound in L^2-norm between the Radon transform and its wavelet approximation, and obtained an estimate of the accuracy of a local image reconstructed from localized Radon data at multiple levels. The current results can be extended to fan-beam and cone-beam geometry.

Iterative reconstruction methods will play a substantial role for better image quality and less radiation dose. In addition to the iterative algorithm described above, a statistical-model-based iterative algorithm was developed for X-ray CT (31). In this case, X-ray CT with low photon counts is viewed as an estimation problem, and it is solved in the maximum likelihood (ML) sense (31). ART-type iterative algorithms are also valuable (54). Theoretical and practical issues with iterative CT algorithms include regularization and acceleration (55–57).

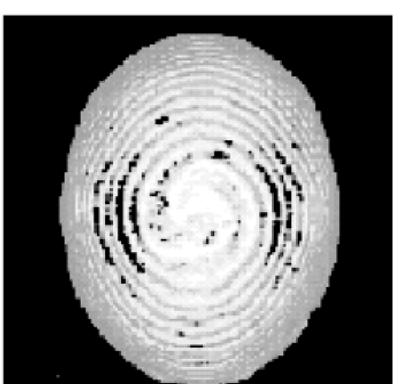

Figure 23. Stairstep artifacts in a surface-rendered view of an adult skull reconstructed with spiral CT.

Progress in hardware will broaden horizons of CT applications. During the past decade, X-ray tubes were greatly enhanced. The availability of highly brillant and collimated synchrotron radiation (SR) pushed spatial resolution into the micron domain. Using the energy tunability of SR, elemental composition of materials can be studied in 3-D. Various area detectors accelerated data acquisition. Techniques of X-ray sources, detectors, and other relevant hardware will be further developed. In particular, computing technologies are in rapid development. All of these will be directly translated into better CT peformance and suggest more CT applications.

With dramatic refinement in CT resolution, volumetric image analyses and visualization are altering clinical practice. For example, Gastrointestinal (GI) tract examination with X-ray CT is currently performed by slice-based visual inspection despite the volumetric nature of the anatomical components, tumors, and lesions. Recently, spiral CT virtual colonoscopy is being actively pursued for colon cancer screening, in which a convoluted large intestine in a spiral CT image volume is interactively explored in a "fly-through" fashion, and may be explicitly mapped onto an elongated planar display. Spiral CT angiography is another example.

Among further readings, introductory descriptions of CT principles can be found in Russ (58) and Parker (59), various applications and practical algorithms with detailed derivations can be found in Herman (60,61) and Kak and Slaney (13), and a rigorous mathematical treatment in Natterer (5). A history of radiological tomography can be found in Webb (62). Articles on CT are published in many journals, such as *SIAM Journal on Applied Mathematics, SIAM Journal on Optimization, Proceedings of IEEE, IEEE Transactions on Image Processing, IEEE Transactions on Signal Processing, IEEE Transactions on Information Theory, IEEE Transactions on Medical Imaging, IEEE Transactions on Nuclear Science, Medical Physics, Physics in Medicine and Biology, Journal of the Optical Society of America, Optical Engineering, Applied Optics, Journal of Scanning Microscopy, Journal of Computer Assisted Tomography,* and *Radiology.*

BIBLIOGRAPHY

1. J. Radon, Über die bestimmung von funktionen durch ihre integralwerte längs gewisser mannigfaltigkeiten. *Ber. Sach. Akad. Wisse.,* **69**: 262–267, 1917.
2. G. N. Hounsfield, *A method of an apparatus for examination of a body by radiation such as X-ray or gamma radiation.* U.S. Patent Specification 1,283,915, 1972.
3. A. M. Cormack, Representation of a function by its line integrals, with some radiological applications. *J. Appl. Phys.,* **34**: 2722, 1963.
4. A. M. Cormack, Representation of a function by its line integrals, with some radiological applications, 2. *J. Appl. Phys.,* **35**: 2908, 1964.
5. F. Natterer, *The Mathematics of Computerized Tomography.* New York: Wiley, 1986.
6. I. Mori, *Computerized tomographic apparatus utilizing a radiation source.* U.S. Patent No. 4,630,202, 1986.
7. W. A. Kalender, W. Seissler, E. Klotz, and P. Vock, Spiral volumetric CT with single-breathhold technique, continuous trans-

port, and continuous scanner rotation, *Radiology,* **176**: 181–183, 1990.

8. C. R. Crawford and K. F. King, Computed tomography scanning with simultaneous patient translation, *Med. Phys.,* **17**: 967–982, 1990.
9. Y. Liang and R. A. Kruger, Dual-slice spiral versus single-slice spiral scanning: Comparison of the physical performance of two computed tomography scanners, *Med. Phys.,* **23**: 205–220, 1996.
10. E. L. Ritman, R. A. Robb, and L. D. Harris, *Imaging Physiological Functions: Experience with the Dynamic Spatial Reconstructor.* New York: Praeger, 1985.
11. D. P. Boyd and M. J. Lipton, Cardiac computed tomography, *Proc. IEEE,* **71**: 298–307, 1983.
12. G. Wang, T. H. Lin, and P. C. Cheng, A derivative-free noncircular fan-beam reconstruction formula, *IEEE Trans. Image Process.,* **2**: 543–547, 1993.
13. A. C. Kak and M. Slaney, *Principles of Computerized Tomographic Imaging.* New York: IEEE Press, 1987.
14. A. Polacin, W. A. Kalender, and G. Marchal, Evaluation of section sensitivity profiles and image noise in spiral CT, *Radiology,* **185**: 29–35, 1992.
15. A. A. Kirillov, On a problem of I. M. Gel'fand. *Sov. Math. (Engl. Transl.),* **2**: 268–269, 1961.
16. H. K. Tuy, An inversion formula for cone-beam reconstruction, *SIAM J. Appl. Math.,* **43**: 546–552, 1983.
17. B. D. Smith, Image reconstruction from cone-beam projections: Necessary and sufficient conditions and reconstruction methods, *IEEE Trans. Med. Imaging,* **MI-4**: 14–28, 1985.
18. P. Grangeat, Mathematical framework of cone beam 3d reconstruction via the first derivative of the Radon transform. In G. T. Herman, A. K. Louis, and F. Natterer (eds.), *Mathematical Methods in Tomography.* New York: Springer-Verlag, 1990.
19. B. D. Smith and J. X. Chen, Implementation, investigation, and improvement of a novel cone-beam reconstruction method, *IEEE Trans. Med. Imaging,* **MI-11**: 260–266, 1992.
20. Y. Weng, G. L. Zeng, and G. T. Gullberg, A reconstruction algorithm for helical cone-beam SPECT. *IEEE Trans. Nucl. Sci.,* **40**: 1092–1101, 1993.
21. G. L. Zheng and G. T. Gullberg, A cone-beam tomography algorithm for orthogonal circle-and-line orbit, *Phys. Med. Biol.,* **37**: 563–577, 1992.
22. M. Defrise and R. Clack, A cone-beam reconstruction algorithm using shift-variant filtering and cone-beam backprojection, *IEEE Trans. Med. Imaging,* **13**: 186–195, 1994.
23. H. Kudo and T. Saito, Derivation and implementation of a cone-beam reconstruction algorithm for nonplanar orbits, *IEEE Trans. Med. Imaging,* **13**: 196–211, 1994.
24. C. Axelsson and P. E. Danielsson, Three-dimensional reconstruction from cone-beam data in $O(n^3 \log n)$ time, *Phys. Med. Biol.,* **39**: 477–491, 1994.
25. H. Hu, An improved cone-beam reconstruction algorithm for the circular orbit, *J. Scanning Microsc.,* **18**: 572–581, 1996.
26. G. L. Zeng, R. Clack, and G. T. Gullberg, Implementation of Tuy's cone-beam inversion formula, *Phys. Med. Biol.,* **39**: 493–507, 1994.
27. R. B. Marr, C. Chen, and P. C. Lauterbur, On two approaches to 3D reconstruction in NMR zeugmatography. In G. T. Herman and F. Natterer (eds.), *Mathematical Aspects of Computerized Tomography,* Berlin: Springer-Verlag, 1981.
28. P. R. Edholm and G. T. Herman, Linograms in image reconstruction from projections, *IEEE Trans. Med. Imaging,* **6**: 301–307, 1987.
29. G. Wang, T. H. Lin, P. C. Cheng, and D. M. Shinozaki, A general cone-beam reconstruction algorithm, *IEEE Trans. Med. Imaging,* **12**: 486–496, 1993.
30. L. A. Feldkamp, L. C. Davis, and J. W. Kress, Practical cone-beam algorithm, *J. Opt. Soc. Am.,* **1**(A): 612–619, 1984.
31. K. Lange and R. Carson, EM reconstruction algorithms for emission and transmission tomography, *J. Comput. Assist. Tomogr.* **8**: 306–316, 1984.
32. D. L. Snyder, T. J. Schulz, and J. A. O'Sullivan, Deblurring subject to nonnegativity constraints, *IEEE Trans. Signal Process.,* **40**: 1143–1150, 1992.
33. I. Csiszàr, Why least squares and maximum entropy? An axiomatic approach to inference for linear inverse problems, *Ann. Stat.* **19**: 2032–2066, 1991.
34. L. K. Jones and C. L. Byrne, General entropy criteria for inverse problems, with applications to data compression, pattern classification and cluster analysis, *IEEE Trans. Inf. Theory,* **36**: 23–30, 1990.
35. G. Wang et al., Spiral CT image deblurring for cochlear implantation, *IEEE Trans. Med. Imag.,* 1998 (in press).
36. L. N. Rothenberg and K. S. Pentlow, Radioation dose in CT, *RadioGraphics,* **12**: 1225–1243, 1992. AAPM Tutorial.
37. P. L. McGhee and S. Humphreys, Radiation dose associated with spiral computed tomography, *Can. Assoc. Radiol. J.* **45**: 124–129, 1994.
38. G. Wang and M. W. Vannier, Longitudinal resolution in volumetric x-ray CT—Analytical comparison between conventional and helical CT, *Med. Phys.,* **21**: 429–433, 1994.
39. W. A. Kalender, A. Polacin, and C. Süss, A comparison of conventional and spiral CT: An experimental study on detection of spherical lesions, *J. Comput. Assist. Tomogr.* **18**: 167–176, 1994.
40. G. Wang and M. W. Vannier, Helical CT image noise—Analytical results, *Med. Phys.,* **20**: 1635–1640, 1993.
41. G. Wang and M. W. Vannier, Low-contrast resolution in volumetric x-ray CT—Analytical comparison between conventional and spiral CT, *Med. Phys.,* 1997, in press.
42. J. Hsieh, Analysis of the temporal response of computed tomography fluoroscopy, *Med. Phys.,* 1997, in press.
43. J. Hsieh, Image artifacts, causes, and correction, In L. W. Goldman and J. B. Fowlkes (eds.), *Medical CT and Ultrasound: Current Technology and Applications.* Madison, WI: Advanced Medical Publishing, 1995.
44. P. M. Joseph and C. Ruth, A method for simultaneous correction of spectrum hardening artifacts in ct images containing both bone and iodine. *Med. Phys.,* **24**: 1629–1634, 1997.
45. P. M. Joseph and R. D. Spital, A method for correcting bone induced artifacts in computed tomography scanners. *Med. Phys.,* **2**: 100–108, 1978.
46. P. M. Joseph and R. D. Spital, The effects of scatter in x-ray computed tomography. *Med. Phys.,* **9**: 464–472, 1982.
47. G. Wang, M. W. Skinner, and M. W. Vannier, Temporal bone volumetric image deblurring in spiral CT, *Acad. Radiol.,* **2**: 888–895, 1995.
48. C. R. Crawford, K. F. King, C. J. Ritchie, and J. D. Godwin, Respiratory compensation in projection imaging using a magnification and displacement model, *IEEE Trans. Med. Imaging,* **15**: 327–332, 1996.
49. G. Wang, D. L. Snyder, J. A. O'Sullivan, and M. W. Vannier, Iterative deblurring for CT metal artifact reduction, *IEEE Trans. Med. Imaging,* **15**: 657–664, 1996.
50. G. Wang and M. W. Vannier, Stair-step artifacts in three-dimensional helical CT—An experimental study, *Radiology,* **191**: 79–83, 1994.

51. G. Wang and M. W. Vannier, Optimal pitch in spiral computed tomography, *Med. Phys.,* **24**: 1635–1639, 1997.
52. T. Olson and J. DeStefano, Wavelet localization of the Radon transform, *IEEE Trans. Signal Process.,* **42**: 2055–2067, 1994.
53. S. Y. Zhao, G. Welland, and G. Wang, Wavelet sampling and localization schemes for the Radon transform in two dimensions, *SIAM J. Appl. Math.,* 1997, in press.
54. Y. Censor and G. T. Herman, On some optimization techniques in image reconstruction from projections, *Appl. Numer. Math.,* **3**: 365–391, 1987.
55. G. L. Herman and L. B. Meyer, Algebraic reconstruction techniques can be made computationally efficient, *IEEE Trans. Med. Imaging,* **12**: 600–609, 1993.
56. J. A. Browne, J. M. Boone, and T. J. Holmes, Maximum-likelihood X-ray computed tomography. *Appl. Opt.,* **34**: 5199–5209, 1995.
57. S. H. Manglos, G. M. Gagne, A. Krol, F. D. Thomas, and R. Narayanaswamy, Transmission maximum-likelihood reconstruction with ordered subsets for cone beam CT, *Phys. Med. Biol.,* **40**: 1225–1241, 1995.
58. J. C. Russ, *The Image Processing Handbook.* Boca Raton, FL: CRC Press, 1995.
59. J. A. Parker, *Image Reconstruction in Radiology.* Boca Raton, FL: CRC Press, 1990.
60. G. T. Herman, *Image Reconstruction from Projections—The Fundamentals of Computerized Tomography.* New York: Academic Press, 1980.
61. G. T. Herman, *Image Reconstruction from Projections—Implementation and Applications.* New York: Springer-Verlag, 1979.
62. S. Webb, *From the Watching of Shadows.* New York: Adam Hilger, 1990.

GE WANG
MICHAEL W. VANNIER
University of Iowa

COMPUTERIZED TRANSACTION INTERCHANGE.

See ELECTRONIC DATA INTERCHANGE.

COMPUTER KEYBOARDS.

See KEYBOARDS.

COMPUTER MEMORY HIERARCHY.

See MEMORY ARCHITECTURE.

COMPUTER MOTION ANALYSIS.

See MOTION ANALYSIS BY COMPUTER.